Alexander Korneev, Alexander Semenov, Denis Vodolazov, Gregory N. Gol'tsman, and Roman Sobolewski

9 Physics and operation of superconducting single-photon devices

Abstract: The chapter reviews the main aspects of the physics of operation and performance of superconducting single-photon detectors (SSPDs) based on, mostly NbN, nanostripe meander-type structures and operated well below the superconductor transition temperature. We present theoretical models developed to describe the photoresponse of superconducting nanostripes, as well as discuss mechanisms of SSPD generation of both photon-detection signals and dark counts. We also outline a standard SSPD fabrication process and discuss basic experimental techniques of SSPD characterization, focusing on the demonstration of its single-photon sensitivity and detection efficiency, as well as on measurements of the timing jitter. Finally, we give an outlook of future research directions and a quick overview of the vast area of SSPD applications.

9.1 Introduction: what is a superconducting single-photon detector

The concept of a superconducting single-photon detector (SSPD), also known as superconducting nanowire single-photon detector (SNSPD),[1] was first introduced and experimentally demonstrated in 2001 in [1], while the first model of SSPD operation was presented in [2]. A SSPD is essentially a superconducting nanostripe with a thickness of several nanometers (typically $\approx$ 4 nm) and a width on the order of 100–250 nm. In practical devices, the nanostripe, initially patterned as a simple straight line (Figure 9.1a) [3] is typically a few-mm-long meander of square [4, 5] or circular shape [6]

Additional address for R Sobolewski: Department of Physics and the Materials Science Graduate Program, University of Rochester, Rochester, NY14627-0231, USA. In addition: Institute of Electron Technology, PL-02668 Warszawa, Poland.

1 The name SNSPD, although quite suggestive and very popular in the literature, is incorrect from the physics point of view, since in all cases presented so far in the literature, the active element is a stripe that can be regarded as 2-dimensional superconductor, but never a nanowire (1-dimensional element).

Alexander Korneev, Alexander Semenov, Gregory N. Gol'tsman, Department of Physics, Moscow State Pedagogical University, 119435 Moscow, Russia, *E-mail:* akorneev@rplab.ru
Denis Vodolazov, Institute for Physics of Microstructures, Russian Academy of Sciences 603950 Nizhny Novgorod, GSP-105, Russia
Roman Sobolewski, Department of Electrical and Computer Engineering and Laboratory for Laser Energetics, University of Rochester, Rochester, NY14627-0231, USA

DOI 10.1515/9783110456806-010,

(see Figure 9.1b and c, respectively) with a total area of approx. 100 μm^2. In the literature one sees special meander shapes such as a spiral for better optical coupling [7] (Figure 9.1d), or even parallel connections of many nanostripes which increase detector output signal and lower kinetic inductance [8] (Figure 9.1e). All SSPDs are fabricated on optically transparent dielectric substrates with epitaxial quality surfaces, such as, e.g., Al_2O_3, MgO, or SiO_2-on-Si wafers.

Originally, the effect of single-photon detection was observed in NbN [3], and up to date practical detectors are mostly fabricated from this material [9]. However, the effect itself has been demonstrated using many other materials, such as Nb [10], NbTiN [11, 12], MoRe [13], TaN [14], MgB_2 [15], and amorphous silicides WSi [16] and MoSi [17], and these latter materials have also been used to produce practical devices.

Unlike well-known traditional superconducting bolometers, including the single-photon resolving transition-edge sensor (TES), SSPDs are operated at temperatures well below the critical temperature of a given superconductor and are biased with a transport current very close to the nanostripe critical current I_C at a given temperature. Later on we shall give a more accurate definition of the SSPD I_C value, but, for the moment we will treat it as the maximum current that be can carried by the SSPD nanostripe, while remaining in the superconducting state. The basic mechanism of the SSPD photoresponse is that absorption of a photon by a nanostripe suppresses or destroys its superconductivity in a local region that is smaller, but comparable to the stripe width. This area is traditionally called a "hot spot". After hot-spot formation the stripe can no longer carry the supercurrent bias and locally switches to the resistive state, leading to a transient voltage signal that is detected as a photon count.

The above model provides a good, qualitative description of SSPD operation, however, a more in-depth analysis of the physical mechanisms involved is needed. A complete description of the SSPD photoresponse requires full understanding of the process of photon energy transfer to the superconducting condensate via a hot-spot formation mechanism that includes analysis of the kinetics of coupled systems consisting of Cooper pairs, quasiparticles, and phonons. Subsequent appearance of a resistive state in a 2-dimensional (2D) nanostripe is, in turn, a result of the interplay between the electric field and quasiparticles, as well as topological excitations like vortices. Finally, in practical devices, one has to deal with so-called dark or unwanted counts, i.e., spontaneous voltage transients occurring in a current-biased SSPD even in a device completely isolated/shielded from any external, optical radiation. Mechanisms responsible for dark counts range from fluctuations of the Cooper-pair density, through thermal or quantum activation of magnetic vortices, to excitation of phase-slip centers. Phase slips (2π phase change associated with dissipation of a single flux quantum) are spontaneous topological excitations, characteristic for 1D superconducting nanowires, as described in [18, 19], thus in practical, NbN SSPDs with 2D nanostripes can be neglected and the prevailing mechanism is thermal unbinding of vortex-antivortex pairs [20, 21] with the Cooper-pair density fluctuations contributing only at bias currents very close to I_C [20]. In 2D superconducting materials below the

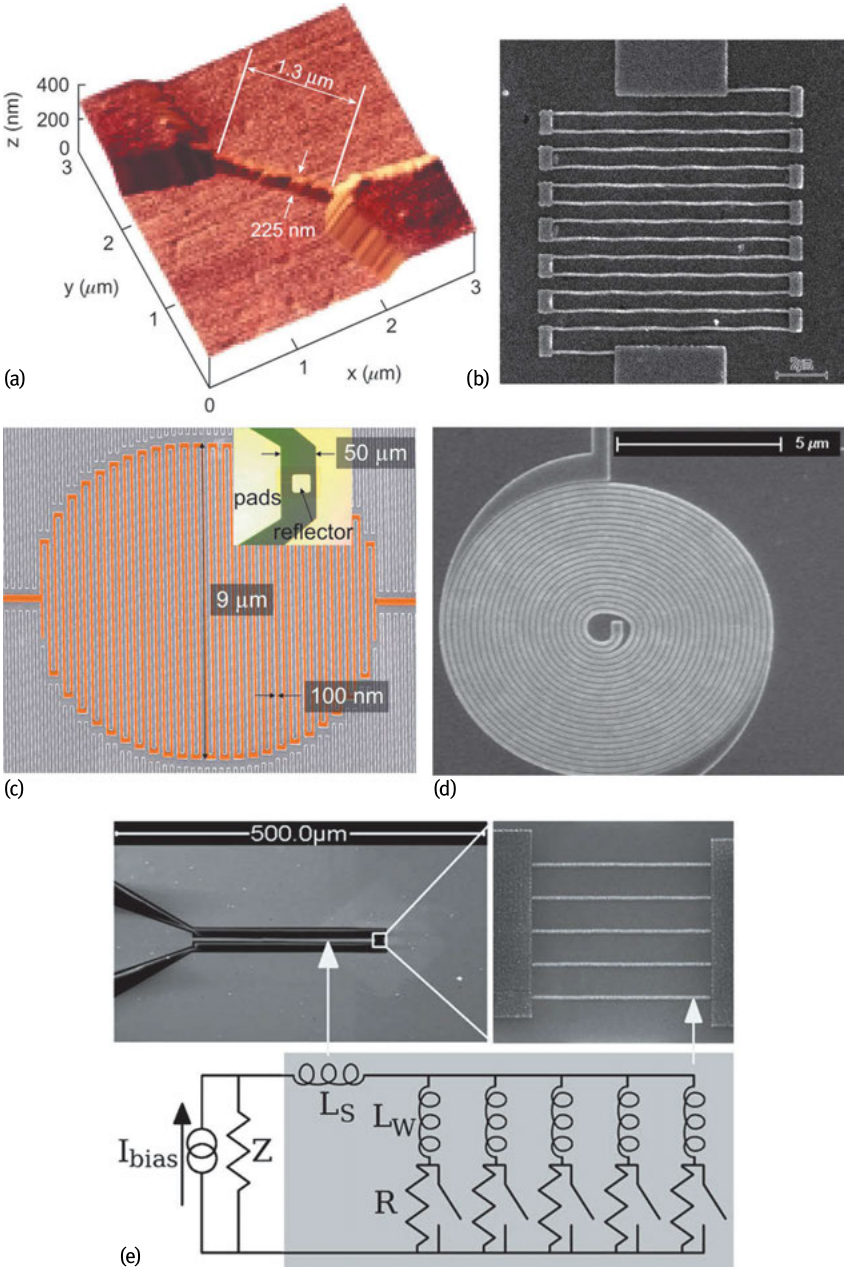

Fig. 9.1: Different configurations of SSPD: (a) single straight stripe between two contacts (a "nanobridge") [3]; (b) early example of the most frequently used meander-shaped stripe covering a rectangular area [4] (for a recent design see Figure 9.8); (c) meander-shaped line covering a circular area which is optimal for coupling to single-mode optical fibers [6]; (d) polarization-insensitive spiral-shaped stripe [7]; (e) multiple stripes connected in parallel providing lower kinetic inductance and faster device operation [8].

Berezinsky–Kosterlitz-Thouless (BKT) transition the formed vortex-antivortex pairs are characterized by a certain binding energy. However, thermal fluctuations that exceed this energy can unbind the vortex pairs leading to appearance of a normal-conducting domain and generation of a voltage-pulse across the SSPD. It is interesting to note that using a ferromagnet/superconductor nanobilayer, e.g., NiCu/NbN, as a nanostripe material leads to substantial reduction of the dark-count rate. The enhancement of pinning in NbN/NiCu bilayers increases binding energy of vortex-antivortex pairs and the dominant mechanism of the observed dark-count transients becomes excitation of single vortices (vortex hopping) near the edge of the 2D nanostripe [21].

Our chapter is focused on the physical aspects of the SSPD photoresponse with the aim of providing a detailed description of both the operation and performance of SSPDs. However, we want to stress here that these devices have already been widely used as detectors for high-performance photon-counting applications, especially for the near-infrared (IR) wavelength range, including the standard communications wavelengths. SSPDs have been very successfully implemented for several applications, ranging from optical debug and testing of very large-scale integrated circuits [22], through characterization of single-photon emitters, to registration of single photons in ultrafast quantum communication systems and quantum cryptography. Detailed information on SSPD applications can be found in [23].

The structure of the chapter is as follows. The next section describes operation principles of the SSPD and presents existing models of both the photon detection and dark counts. Section 9.3 reviews the most popular methods for SSPD fabrication and characterization, and, finally, Section 9.4 gives conclusions, as well as some directions for future research.

9.2 Operational principles of SSPDs

9.2.1 Photoresponse of superconducting nanostripes

Physical process of single-photon detection by a current-carrying superconducting nanostripe could be qualitatively described as follows: a single photon with an energy of approx. 0.6 eV or larger (corresponding wavelength of about 2 μm or shorter) is absorbed by an electron in one place along a superconducting nanostripe that, as a result, is instantaneously excited far above the Fermi energy E_F. In quasiparticle language, a Cooper pair is broken and high-energy electron-like and hole-like quasiparticle excitations are created. Next, because of electron-electron (e–e) and electron-phonon (e–ph) interactions this high-energy electron relaxes via excitation of lower energy nonequilibrium electrons and phonons. We stress that in conventional, metallic superconductors, such as, e.g., NbN, the Cooper pair bonding energy, i.e., the superconducting energy gap Δ, is in the range of 1–2 meV, much smaller than the in-

cident photon energy, and the photoresponse (electron energy relaxation) process is practically the same for either normal or superconducting materials, as long as the average energy of nonequilibrium electrons/quasiparticles is larger than several Δ [24, 25].

Let us now discuss clean or pure materials, where at energies smaller than the Debye energy Ω_D, the e–e relaxation rate $1/\tau_{e-e}$ is much smaller than $1/\tau_{e-ph}$. Under such conditions, relaxation is dominated by the e–ph process, and within picoseconds (less than one picosecond for materials with $\Omega_D \sim 30$ meV ~ 350 K) practically all initial photon energy is transferred from the quasiparticle to the phonon subsystem [24, 25], so nonequilibrium phonons, in turn, can re-excite nonequilibrium quasiparticles and/or break Cooper pairs. In the absence of escape of nonequilibrium phonons from the stripe to the substrate, within the hot spot, phonon and electron subsystems are thermalized with some characteristic thermalization time τ_{th}. At $t > \tau_{th}$ both subsystems reach the common, quasi-nonequilibrium temperature $T_{neq} > T_{bath}$, where T_{bath} is the bath temperature of our sample. In other words, at a time on the order of τ_{th} from the initial excitation, the number of quasiparticles reaches its maximum value which corresponds to the maximum suppression of Δ within the hot-spot region. If we include diffusion of nonequilibrium quasiparticles out of the center of the hot spot, its size will grow during the thermalization process. The latter leads to a lower value of T_{neq}, or, equivalently, to a smaller number of quasiparticles per unit volume of the hot spot.

Taking the above considerations into account, we can estimate the incident photon energy needed to create a hot spot with a fully suppressed (nonsuperconducting) center and radius $R_{spot} = L_{th} = (D\tau_{th})^{1/2}$ (where D is a diffusion coefficient) as

$$E_{photon} = d\pi L_{th}^2 (N(0)\Delta^2/2 + \pi^2 N(0)(k_B T_c)^2/3(1 + C_{ph}(T_c)/C_e(Tc)/2)) , \qquad (9.1)$$

where d is nanostripe thickness, $N(0)$ is the density of states of quasiparticles per spin at the Fermi energy, and $C_{ph}(T_c)$ and $C_e(T_c)$ are the heat capacities of phonons and quasiparticles, respectively, at $T = T_c$. Since we have assumed a nonsuperconducting hot-spot center ($\Delta = 0$), both quasiparticles and phonons reach the same temperature $T_{neq} = T_c$. In Equation (9.1), the first term in the brackets corresponds to the energy of the superconducting condensate, while the second and third ones are related to the energy of quasiparticle and phonon subsystems, respectively. Equation (9.1) was derived using a spherical Fermi surface and the Debye model for phonons. For typical parameters of the NbN detector: $N(0) = 25.5\,\mathrm{nm^{-3}eV^{-1}}$, $k_B T_c = 0.86$ meV, $\Delta = 1.76 k_B T_c = 1.51$ meV, $C_{ph}(T_c)/C_e(T_c) = 1.2$ (at $T_c = 10$ K), $d = 4$ nm, $D = 0.5\,\mathrm{cm^2 s^{-1}}$, and assuming that $\tau_{th} \approx 7$ ps, we find $E_{photon} = 0.57$ eV which corresponds to the wavelength $\lambda = 2200$ nm. Thus, photons with energies of at least 1.14 eV would create normal spots with a large enough diameter, since the condition $T_{neq} = T_c$ is fulfilled only at $2R_{spot} > 2L_{th}$, as could be seen from Equation (9.1). Conversely, photons with smaller energies by the time $t = \tau_{th}$ would not be able to create a completely normal spot, instead the spot would have a radius $R_{spot} = L_{th}$ with a partially suppressed Δ.

Equation (9.1) and the associated physical picture are based on the energy conservation law and the photon's energy down-conversion process [24–26]. The excited electron energy relaxation process has been presented using kinetic equations, assuming, as we stressed before, the pure metal condition with $1/\tau_{e-e} \ll 1/\tau_{e-ph}$ at $\varepsilon < \Omega_D$, and for a spatially uniform case [for such materials, one may expect that $\tau_{th} \sim \tau_{e-ph}(T_c)$].

We need to admit here that all superconducting materials that have demonstrated an ability to detect single photons are, actually 'dirty' metals with a very short mean path and fast e–e relaxation, i.e., $1/\tau_{e-e} \gg 1/\tau_{e-p}$ in a wide energy interval. Thus, one may expect that in this case $\tau_{th} \sim \tau_{e-e}(T_c)$ is much shorter than $\tau_{e-ph}(T_c)$ – the τ_{th} relaxation time characteristic for the pure material case.

Let us now discuss how narrow a superconducting nanostripe needs to be in order to successfully record an incident photon. If Δ were actually zero inside the hot spot and, simultaneously, the stripe width w were less than or equal to the hot-spot size, the detection process would be very simple, since absorption of a photon would turn a cross-section of the stripe resistive and for any bias current a voltage signal could be detected. In reality, however, neither of the above cases is typically satisfied. An estimated hot-spot size for NbN upon absorption of an optical photon is $2L_{th} \approx 50$ nm; thus, is a factor 2-to-4 smaller than w of routinely fabricated SSPDs. The latter is due to the fact that stripes narrower than 80–100 nm are very difficult to be reproducibly fabricated, if they need to be very uniform over the length of ~ 0.5 mm, as is needed for $10 \times 10\ \mu m^2$ meander structures. Independently, complete suppression of Δ inside an NbN hot spot is, according to our discussion in connection with Equation (9.1), impossible to achieve in the case of IR photons with λ greater than $1.1\ \mu m$.

Nevertheless, we know very well, based on the countless experiments that single IR photons are efficiently counted using 100-nm and wider nanostripes. The only requirement is that one needs to bias the stripe with a sufficiently large supercurrent I_B. When the hot spot appears across the nanostripe, its I_C reduces from I_C^{stripe} down to $I_C^{spot} < I_C^{stripe}$. Therefore, if I_B is in the range $I_C^{spot} < I_B < I_C^{stripe}$, the superconducting nanostripe switches to a resistive state after absorption of the photon. Then, due to a large Joule heating, the resistive domain grows in time, eventually resulting in a large, easily detectible voltage drop across the device. Note that the presence of a hot spot with fully suppressed Δ provides $I_C^{spot} = 0$ only when $w \le 2L_{th}$. If $w > 2L_{th}$, the resistive state appears at a finite I_B that could be estimated as

$$I_C^{spot} = I_C^{stripe}(1 - 2R_{spot}/w)\,, \tag{9.2}$$

assuming that the hot-spot presence simply reduces the effective width of a superconducting stripe and the current in the stripe is uniformly distributed.

If one takes into consideration a current redistribution effect within a nanostripe – well known for superconducting stripes with 'obstacles' [27] – the superconducting state can be destroyed in such case when a local current near the hot spot exceeds the value of the de-pairing current I_{dep}, i.e., the maximum current that can flow in a

superconductor without dissipation, and the expression for I_C^{spot} can be written as [28]

$$I_C^{spot} = I_{dep}[1 - (2R_{spot}/w)^2]/[1 + R_{spot}/(R_{spot} + \xi)] , \tag{9.3}$$

where ξ is the superconducting coherence length. Physically, the situation resembles current redistribution in a normal, metallic stripe with inclusion of a local, fully insulating spot. In both cases, the current density distribution is inhomogeneous with a local maximum near the spot. Equation (9.3) was obtained with the help of a solution of the Laplace equation for the phase of the superconducting order parameter, in analogy to the electrostatic potential in a problem with the current flowing in a normal-metal stripe with an insulating inclusion. Above I_{dep} the superconducting state becomes unfavorable because the kinetic energy of Cooper pairs exceeds their coupling energy. In a real stripe, I_C^{stripe} is always smaller than I_{dep} due to the presence of stripe defects, nonuniformities, or fluctuations.

In the above considerations, we have assumed that inside the hot spot $\Delta = 0$, but, in fact, photon detection is possible even if photon absorption creates a hot spot with partially suppressed Δ. Again the situation is similar to the case of a metallic stripe with a localized (significantly smaller than the stripe width w) inclusion that is not fully insulating, but a highly resistive region. This case also leads to an extra current concentration on the sides of the inclusion. This effect is, however, significantly smaller as compared to the case of a completely insulating inclusion. In the case of a superconducting stripe, the above situation leads to an enhanced value of I_C^{spot}. At the same time creation of such a weakly superconducting region requires smaller photon energy, because electrons and phonons do not have to be heated up to T_c and Δ remains nonzero. Using a step-like spatial dependence of Δ one may find the following

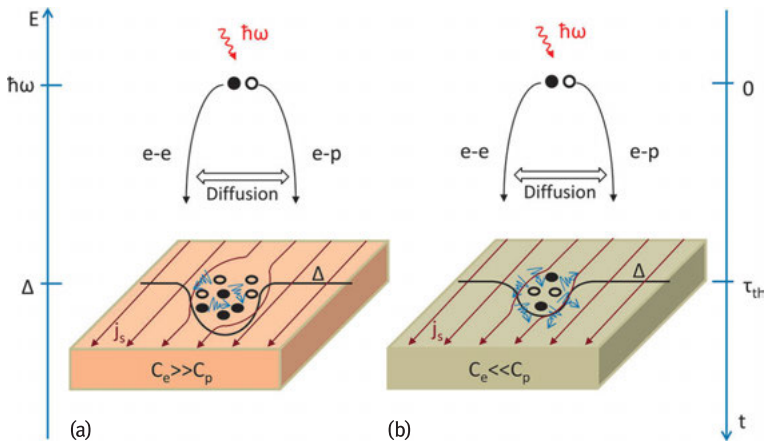

Fig. 9.2: Schematic representation of a chain of events leading to the SSPD photon-detection event in the case of a superconducting material with either (a) $C_e \gg C_p$ or (b) $C_e \ll C_p$.

expression:

$$I_C^{spot} = I_{dep}[1-(2R_{spot}/w)^2(1-\gamma^2)/(1+\gamma^2)]/\{1+R_{spot}(1-\gamma^2)/[(R_{spot}+\xi)(1+\gamma^2)]\}, \quad (9.4)$$

where $\gamma = \Delta_{in}/\Delta_{out}$ is equal to the ratio of Δ's inside and outside of the hot spot, respectively [28].

We stress that Equations (9.3) and (9.4) were derived under the assumption that a hot spot was located at the center of the superconducting nanostripe. However, this may not be the case and in practice it turns out that I_C^{spot} is dependent on the hot-spot position within the nanostripe. Calculations in [28, 29] show that I_C^{spot} reaches its minimum or maximum value depending on whether the hot spot either touches the edge of a stripe or is located at the stripe center, respectively. This result originates from a different current flow around the hot spot and it, obviously, has a direct consequence for SSPD performance. For example, it means that there is a finite interval of biasing currents where the SSPD intrinsic detection efficiency[2] (IDE) changes from 0 to unity, and this is an intrinsic characteristic of a given, practical device [29].

The main features of the SSPD photoresponse mechanism discussed above are summarized in Figure 9.2. Briefly, a photon with the energy $\hbar\omega$ creates a pair of quasiparticles (one electron-like and one hole-like) that due to the e–e and e–ph interactions and diffusion lead to a "cloud" of low-energy quasiparticles and phonons forming at time τ_{th} a local hot spot with either suppressed or destroyed Δ. Formation of a hot spot forces the bias supercurrent flow around it. Figure 9.2a corresponds to a situation where $C_e(T_C)$ is large compared to the phonon $C_p(T_C)$ value and most of the photon energy is transferred to quasiparticles. Conversely, Figure 9.2b represents the opposite limit, i.e., $C_p \gg C_e$, in which the number of created quasiparticles is smaller due to a larger energy transfer to the phonon system. As a result, in the second case, the size of the hot spot (its diameter $2R_{spot}$) and suppression of Δ are smaller, which leads to a larger value of I_C^{spot} (see Equation (9.4)) and at fixed I_B it provides a smaller IDE value, as compared to Figure 9.2a.

We want to emphasize that due to the absence in the literature of a rigorous description of a superconducting nanostripe in the photo-induced nonequilibrium state, based on the kinetic equations with incorporation of quasiparticle diffusion, Equations (9.1), (9.3), and (9.4) have to be regarded only as a qualitative estimation. In addition to our approach, there are also various phenomenological models that relate the size of a hot spot to the incident photon energy and the corresponding I_C^{spot}

2 Intrinsic detection efficiency (IDE) is a probability of detection event normalized to the number of *absorbed* photons. IDE is often called quantum efficiency (QE). If IDE = 1 every absorbed photon produces a measurable detection event although the ratio of absorbed photons to incident photons may still be well below unity depending on the absorption of the meandering nanostripe. In the latter case, we can talk about detection efficiency (DE), i.e., probability of detection event normalized to the number of incident photons. When a system of photon delivery to the detector is included, e.g., fiber coupling, DE becomes a system detection efficiency (SDE).

value [2, 30–34]. Many of these works are actually based on the Rothwarf–Taylor equations [35] that deal with the number of nonequilibrium quasiparticles and phonons created in a superconductor by photon absorption. Part of the incident photon energy that is transferred to nonequilibrium phonons is usually described by a parameter $\eta < 1$ and time τ_{th} has meaning as a phenomenological parameter, related to $\tau_{\text{e–e}}$. Some of these models even predict that partial suppression of Δ inside the hot spot leads to an increase of $I_{\text{C}}^{\text{spot}}$ in comparison with the same hot spot but with fully suppressed Δ. Unfortunately, none of these models, including our approach, can predict, e.g., what superconducting material would be the optimal as an active nanostripe element; thus, they are phenomenological in nature and can only explain/model the experimentally observed SSPD performance.

9.2.2 SSPDs in an external magnetic field

It turns out that the presence of the magnetic field H can shed a new light on the physics of the nanostripe photoresponse mechanism. The main reason is that a weak magnetic field, while it does not create any vortices in a superconducting stripe, can modify current distribution across the stripe due to screening currents. Current phenomenological models of SSPD operation are based on the assumption that an absorbed photon creates a hot spot with a diameter that is smaller [2, 28–34] or equal [36] to width w of the stripe. The hot-spot region that extends over the entire w of the stripe can be considered as a weak link and application of the external magnetic field should decrease $I_{\text{C}}^{\text{spot}}$. The latter suggests that, if the above model is correct, the value of IDE measured at a given I_{B} should shift to lower currents with increasing H. Calculations performed in the case when the hot-spot size was smaller than w resulted in a complicated dependence of IDE on both I_{B} and H [37]. It has been found that in high-quality NbN devices characterized by the IDE value not far from unity there is a certain bias level I_{cross}, at which for $I_{\text{B}} > I_{\text{cross}}$ IDE decreases in the magnetic field, while for $I_{\text{B}} < I_{\text{cross}}$ the IDE increases as shown in Figure 9.3. The effect is, apparently, associated with the fact that the value of $I_{\text{C}}^{\text{spot}}$ depends in this case on a hot-spot position along the stripe width and it has been experimentally observed in [38]. In addition, theoretical modeling was able to explain an intriguing observation that the applied magnetic field has a more pronounced impact on SSPDs operating at long (IR) wavelengths [37, 39, 40]. According to [37], a photon with larger energy creates a hot spot large enough with a strongly suppressed Δ that is able to pin vortices and because of that, the $I_{\text{C}}^{\text{spot}}$ becomes less sensitive to relatively weak magnetic fields. The latter can be seen in Figure 9.3, where hot spots of different radiuses correspond to absorption of photons with different energies.

SSPD models and experiments that include magnetic field also help to clarify the impact of stripe bends on photon detection in meander-type detectors. In an experiment with an SSPD that, contrary to conventional meander geometry, contains a

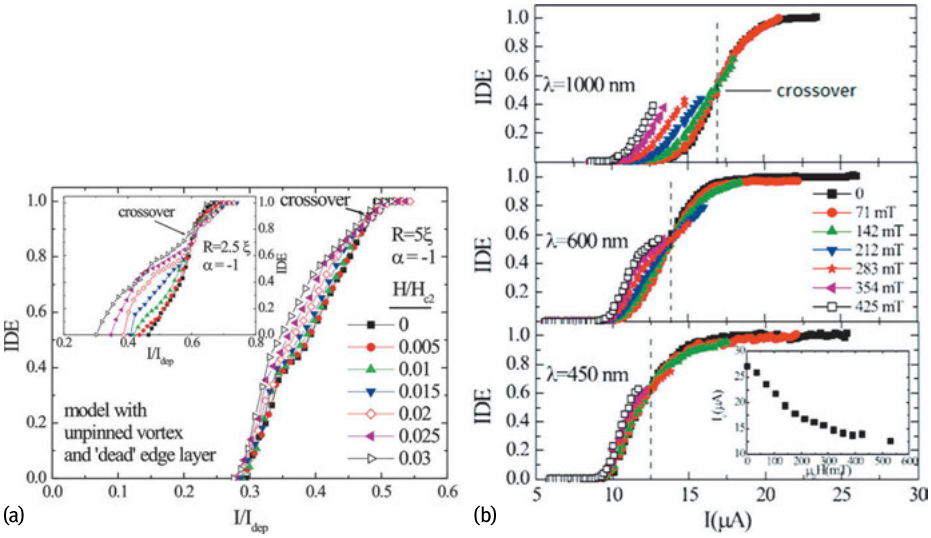

Fig. 9.3: SSPD IDE dependence on the bias current normalized to the depairing current at different magnetic field values [37]. (a) Hot spot model calculations with the radius $R_{spot} = 5\xi$. The inset shows the same case but with $R_{spot} = 2.5\xi$. (b) Experimental results for an NbN SSPD operated at three different wavelengths (photon energies). Curves corresponding to the strongest fields can be broken before reaching the expected crossover current due to the critical current limitation, see the inset.

quadratic Archimedean spiral, i.e., a structure that has bends with only one curvature, it has been observed that IDE depends not only on the H value, but also on its sign/direction [41]. The effect was clearly visible in devices operating at IDE $\ll 1$, and for photons with relatively large wavelengths. The latter indicates that such photons, apparently, cannot effectively pin the vortices. Apparently, depending on its direction, H induces near the inner corner of the bend screening currents that either enhance or prevent vortex entry into the stripe and this way it influences the IDE value.

Finally, we comment on the role of vortices in SSPD operation. It is well known that current-biased superconducting stripes with w's greater than several coherence lengths can be transferred into the resistance state due to the penetration and motion of Abrikosov vortices. The vortices are created inevitably as soon as their entrance into the stripe becomes energetically favorable, i.e., when the energy barrier for vortex entry becomes zero. This barrier, however, decreases with the increase of the stripe transport current, because the current tends to move vortices across the stripe via a Lorentz force. The value of the current at which the barrier is equal to zero is, by definition, the stripe $I_B = I_C$ and, quantitatively, the I_C density equals the de-pairing current density for a defect-free stripe. When I_C becomes suppressed during hot-spot formation, the vortices enter into the stripe and start moving, producing resistance and, as a result, a measurable voltage pulse.

9.2.3 Origin of dark counts in SSPDs

The vortex energy barrier, mentioned at the end of the previous section, can be overcome and vortices can enter into the stripe even when $I_B < I_C$ with the help of thermal or quantum fluctuations Physically, this means that there exists a finite probability of a vortex entry and subsequent formation of a resistive state even when there is no incident photon absorption. For a biased SSPD, such a vortex-induced resistive state leads, of course, to a voltage transient that is essentially identical in terms of its width and amplitude to pulses produced by photon absorption, but it appears stochastically even when the detector is completely shielded [10, 42]. These stochastically generated voltage pulses are commonly known as, so-called, false or dark counts and, in general, are an inherent feature of any photon-counting devices. We need to stress, however, that contrary to semiconducting photon counters, such as avalanche photo diodes (APDs), where dark counts, such as after-pulsing, are directly related to the highly nonlinear, threshold-type operation mechanism, in SSPDs, dark or spurious counts are a result of superconducting fluctuations in a 2D nanostripe.

Figure 9.4 presents an example of the dependence of both photon- (Figure 9.4a) and dark counts (Figure 9.4b) on the normalized bias current for the same, meander-type SSPD operated at two different temperatures. The photon-count rate, or, equivalently, the device DE is clearly enhanced at very low temperatures and for high-quality devices (as in this example) tends to saturate as I_B approaches I_C. Conversely, the dark-count rate decreases exponentially with the decrease of the bias and becomes negligible at very low temperatures [43]. Thus, in SSPDs, the dark counts can be easily controlled and set practically to zero if the operating temperature is low enough, or one keeps I below a certain threshold. At the same time the detector performance in terms of DE does not suffer and can, actually be enhanced (see in Figure 9.4 the SSPD operation at 2 K versus 4.2 K at the same wavelength/photon energy).

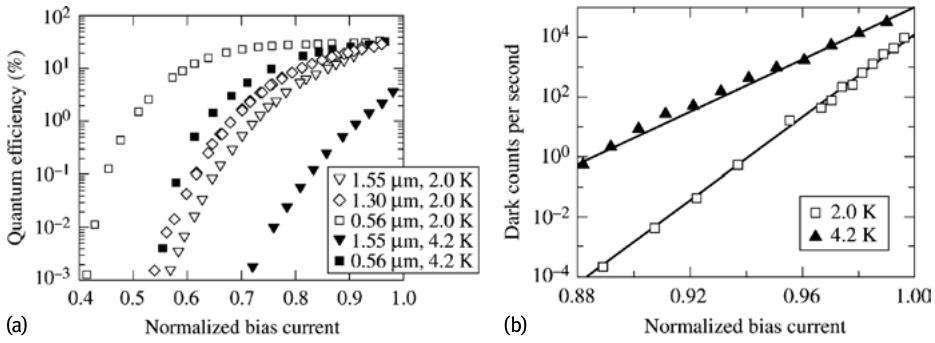

Fig. 9.4: (a) Detection efficiency, or, equivalently, life-photon count rate as a function of the normalized bias current I_B/I_C, measured for an SSPD operated at 4.2 K and 2 K and illuminated with photons of different wavelengths. (b) Dark count rate of the same device measured at 2 K and 4.2 [47].

Theoretical descriptions of dark counts have been discussed in a number of papers, including [44–46] and, as we have mentioned before (see Section 9.1), mechanisms responsible for dark counts range from fluctuations of the Cooper-pair density, through thermal or quantum activation of magnetic vortices, to excitation of phase-slip centers. We have also stressed that in practical SSPDs containing 2D nanostripes and operated under normal conditions (I_B not too close to I_C), the dominant mechanism is vortex-related fluctuations. An intriguing question is whether these fluctuations are in nature classical thermal fluctuations or quantum ones. A number of works in the literature have attempted to identify experimentally the nature of dark counts and, in our opinion, the most consistent approach was presented in a very recent work by Murphy et al. [48]. In this work, the authors extracted dark-count rates from the distribution of switching current probabilities when the SSPD was in current-setting mode and biased by a steadily increasing I_B. Such a measurement has been repeated many times and in each case, when the SSPD switched to the resistive state, a corresponding I_B value was recorded. As a result, one obtains a distribution of the switching currents as a function of the bias. Analyzing this distribution, it has been possible to extract both the true I_C, i.e., the current at which the fluctuation energy barrier that produces the resistive state is zero, as well as the dependence of the fluctuation rate on the current. The resulting dependence is exponential-like and one can parameterize its slope in a logarithmic scale by some temperature T^* that should be equal to the temperature of the film if the fluctuations were strictly thermal. A quantitative analysis of the experimental data was done within the Kurkijarvi–Garg model [49] and it was found that above a certain temperature T_q, of the order of 2 K, the slope has almost a linear dependence, increasing as $1/T$. The latter is expected for thermal fluctuations, however, below T_q the slope ceased increasing and became constant. Since I_C itself has no abnormality at T_q, one can conclude that the plateau effect is not related to the saturation of the electron temperature, but it is, actually, a strong indication that below T_q fluctuations are not thermal, but quantum in nature. In our case, for a 2D stripe, one should expect the Abrikosov vortices to tunnel across the film. An intriguing feature is that above some other temperature $T_m > T_q$, the probability slope starts to increase again, which can be attributed to multiple vortices jumping across the film. The idea is that in the case of low I_B, heat dissipated during a single vortex crossing is not enough to trigger the transition to the resistive state, and at least two or more vortices crossing our 2D stripe at the same place and time are required to trigger the resistive transition. Of course, in the case of at least two simultaneous vortex transitions, the probability of generating a voltage transient is decreased. Figure 9.5 presents the graphs representing the distribution function of standard deviation dependence on temperature, depicting its slope change (Figure 9.5a), as well as the so-called escape temperature T_{es} dependence on the temperature (Figure 9.5b). T_{es} is the temperature that arises while fitting a statistical distribution of switching currents by thermal fluctuations. One can see in Figure 9.5b that T_{es} saturates below T_q and starts to decrease above T_m.

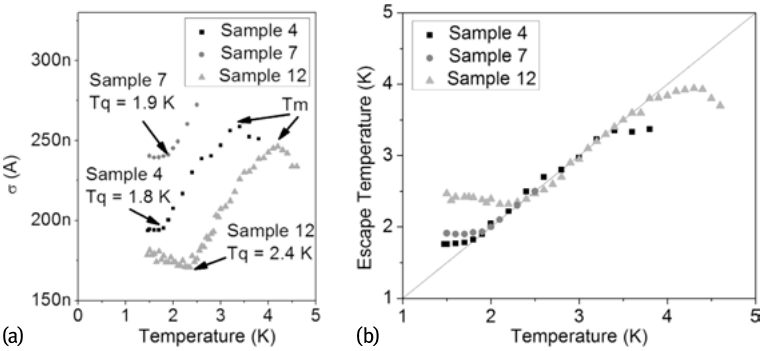

Fig. 9.5: (a) Standard deviations of switching current I_C distributions measured at different temperatures. One can see saturation at low temperatures (below the temperature denoted as T_q) which is a manifestation of macroscopic quantum tunneling. The multiple vortex jumps occur when $T > T_m$. (b) The so-called escape temperature T_{es}, the temperature that arises while fitting the statistical distribution of switching currents by thermal fluctuations at temperature T_{es}, versus natural temperature for three studied samples. One can see that T_{es} saturates below T_q and starts to decrease above T_m [48].

9.2.4 Production of SSPD output voltage pulses

We have already explained how absorption of a photon results in appearance of a resistance in a current-carrying superconducting nanostripe. Now let us focus on the voltage pulse that is produced as the outcome of this event. A typical voltage pulse, recorded by the readout circuit of the NbN SSPD is presented in Figure 9.6. One can note that the pulse has a strongly asymmetric shape with a fast rising edge, followed by a slow decay part. The rising part of the pulse reflects the appearance of the resistive state in a nanostripe that starts at the moment when I_C^{spot} falls below I_B, and the normal component of the current appears. Normal current dissipates power via Joule heating of the stripe; thus, the length of the resistive section of the stripe grows progressively and the total resistance increases. However, in a voltage source bias case, the increase of the resistance causes the decrease of the bias current, reducing Joule heating. Thus, the resistive region does not grow infinitely but reaches some maximum size when the Joule heating flux equals heat dissipation into the SSPD substrate. Correspondingly, the voltage photoresponse pulse reaches its peak value when the stripe resistance approaches the impedance of the readout line. Afterwards, the stripe starts to cool down and its resistive region collapses.

As we can see in Figure 9.6, the voltage pulse decay is much longer than the pulse rise time. For practical, meander-type SSPDs, the origin of this long decay is, actually, not the dynamics of the resistive state collapse, but is due to a very large value of the kinetic inductance L_k of our ultra long and narrow superconducting nanostripe. In superconductors, L_k is a measure of the "inertia" of the superconducting, Cooper-pair condensate, so in the SSPD nanostripe, after the resistive state collapse the supercur-

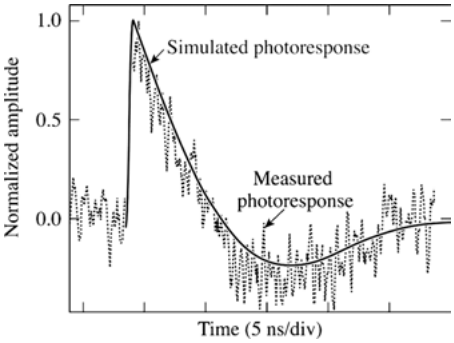

Fig. 9.6: Time-resolved photoresponse of a fiber-coupled, 100-μm^2 area SSPD (dotted line) and the simulated signal (solid line) based on the calculated 420-nH value of the SSPD kinetic inductance. The negative dip of the pulse is due to the limited 0.05–4 GHz bandwidth of the output power amplifier. The amplifier bandwidth was included in the simulations. [50]

rent is recovered with a characteristic time $\tau_{LR} = L_k/R_L$, where R_L is the impedance of an external readout circuitry (typically 50 Ω). For example, for an SSPD meander with a nanostripe of the length of ~0.5 mm (approx. 100 μm^2 detector area), width of 100 nm, and square resistance R_{sq} of about 500 Ω, the voltage transient decay time is about 10 ns, and L_k, extracted by fitting the falling edge of the pulse by a single exponential function, is as large as ~500 nH. The latter value is, actually, in good agreement with the one expected for a dirty superconducting film $L_{sq} = \hbar R_{sq}/(e\Delta)$.

For simulation purposes, the rise time of the SSPD output pulse τ_h can be expressed analogously to τ_{LR}, by replacing R_L with the resistance R_h of the stripe resistive region. One needs to remember, however, that R_h changes with time and because of that the front part of the pulse cannot be fitted by a simple exponential dependence. Moreover, R_h increases with the increase of the length L of the detector, because the larger L corresponds to the larger L_k, and, subsequently, it leads to a larger size of the normal domain (larger R_h). Experimentally, nonlinear dependence of rise time $\tau_h(L) \sim L_k/R_h(L)$ was observed for NbN-based detectors, and calculations made in the framework of the two-temperature model reasonably coincided with an experiment [51]. These calculations give maximal R_h of order 0.5 kΩ for a meander with the length $L = 500\,\mu m$. Thus, the value of R_h corresponded to the length of a nanostripe resistive segment on the order of its width.

The pulse fall time limits the time-domain performance of the SSPD, setting the dead time–the timing parameter important for any photon-counting application. Roughly speaking, it is a period of time after registration of a photon that is needed for the detector to restore its initial state. Although all energy relaxation processes in SSPD evolve on a picosecond time scale, in practical devices the speed of operation is limited by its L_k. One can use the photoresponse pulse duration (practically coincides with its fall time) as a good estimation of the dead time, its accurate quantitative definition requires a better understanding of the processes taking place after photon absorption. A deep insight into this problem was given in [16] and its supplementary materials.

It is important to note that dead time is related not only to the pulse decay time, but also depends on the SSPD DE and I_B. Figure 9.7 schematically illustrates the time evolution of I_B and DE after the photon-detection event. When the photon is detected/absorbed the hot spot is formed and, for a short period of time, the SSPD switches into the resistive state (Figure 9.7a). During this time a voltage signal appears whereas for a voltage-biased device, the current drops rapidly (Figure 9.7b and c). Nominal DE of the device is, of course, in this phase very low: since I_B is low, the SSPD cannot detect a new photon. This is the origin of detector dead time. As time moves on, the voltage transient drops to zero, the superconducting state is recovered, and I_B returns to its nominal value, as is shown in Figure 9.7b and c. In addition, Figure 9.7d shows the time evolution of DE and, simultaneously, compares the behavior of two detectors with different DE(I_B) (see Figure 9.7d inset) dependences: a "good" one with a fast rise

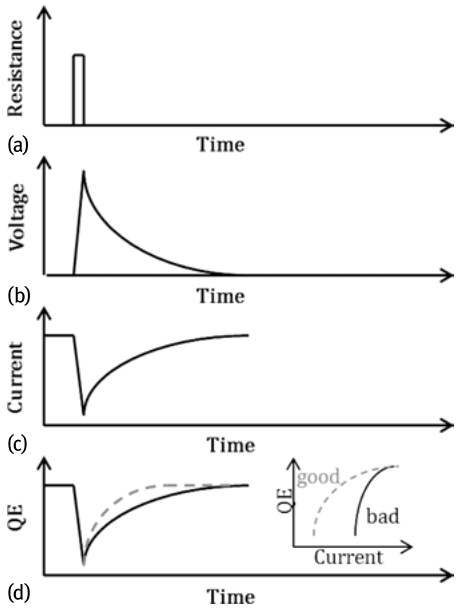

Fig. 9.7: Schematic illustration of the origin of SSPD dead time and its relation to the dependence of DE on I_B, when the device is biased by the voltage source. (a) When a photon is absorbed, a hot spot is formed and the nanostripe becomes resistive for a short period of time. During this time we observe the fast-rising front edge of the photon count voltage pulse (b). Simultaneously, I_B rapidly drops as shown in (c), since its portion has been diverted into the load circuit. The characteristic time of the above processes is $\tau_h = L_k/R_h$. When the stripe resistive region cools down and superconductivity is being restored, the voltage drops (b) and, simultaneously, I_B increases (c) to its initial value, both with the characteristic time $\tau_{front} = L_k/R_L$. The actual dead time is controlled by the dependence of DE on I_B. Panel (d) schematically shows recovery of QE for two different SSPDs with different DE (I_B) dependences (inset): the "good" device (red dashed) and the "bad" one (solid black). The "good" device has higher QE at lower bias currents; thus, its DE recovers faster and the corresponding dead time is shorter.

of DE with current and a "bad" one with a slow rise of DE with current. Naturally, since for the "good" detector DE recovers faster, it will be able to detect photons even if its I_B had not reached its steady value. Thus, such a detector will exhibit a shorter dead time.

The above discussion clearly shows that the main limiting factor of SSPD photon-counting speed is L_k. Since the increase of either the nanostripe w or d is not a practical option due to the resulting sharp reduction of the device DE and the meander size is typically determined by the detector application, i.e., an optical spot size, the good solution is to divide the entire nanostripe into several, small-meander sections connected in parallel [8]. L_k of a meander divided into N parallel sections is reduced N^2 compared to the single meander. Thus, such segmentation allows one to reduce the dead time to a value of the order 100 ps that is limited not by τ_{LR} but by the relaxation time of the resistance state [52].

9.3 Methods of experimental investigation and characterization of SSPDs

9.3.1 SSPD fabrication

SSPDs are typically fabricated from ultrathin superconducting films by traditional methods of electron-beam lithography and reactive ion etching (RIE). In most cases, the films are produced by DC reactive magnetron sputtering on heated substrates, as in the case of NbN, Nb, and NbTiN. Silicide films, such as WSi and MoSi, are usually deposited by co-sputtering from two targets [17, 53].

As an example of the NbN SSPD fabrication process, we are going to follow the procedure presented in Reference [54]. An NbN film was sputtered on a precleaned sapphire or silicon wafer from a metallic Nb target in the $Ar + N_2$ gas mixture with partial pressures of 5×10^{-3} mbar and 10^{-4} mbar for Ar and N_2, respectively. During deposition the substrate was kept at 900°C and the film thickness which typically ranged from 3.5 nm to 10 nm was determined based on the deposition time and the precalibrated deposition rate. In the next step, 100-nm-thick Au alignment marks were produced by standard optical lithography using a AZ1512 photoresist. We also used a 5-nm-thick Ti transitional layer for better adhesion of the gold. Both Ti and Au layers were deposited by resistive evaporation at room temperature. Meanders with, typically, 100-to-250 nm-wide nanostripes were defined by e-beam lithography in positive, PMMA (Poly[methyl methacrylate]) 950 K electron resist, using the toluene-to-isopropanol 1 : 10 mixture as a developer. The choice of the 80-nm thickness of the PMMA 950 K resist, ensured a reliable protection of the superconducting film during the RIE process, while at the same time, such a thin resist allowed us to reliably fabricate stripes as narrow as 80 nm. The RIE process itself was performed in SF_6 gas. In this approach, NbN was removed from the regions of the exposed resist, so the mini-

mal width of the superconducting stripe did not depend directly on the electron beam diameter, but was mainly determined by scattering in the photoresist. Finally, the device contact pads were fabricated in the same manner as the above-mentioned alignment marks. The contact pads formed a shorted end of a coplanar waveguide used to deliver the detector photoresponse pulse to the read-out circuitry. For a process-flow schematics, see Table II in Reference [54].

Our best, meander-type detectors covered the area of either 10×10 or $4 \times 4\ \mu m^2$ with a filling factor (the ratio of the area occupied by the superconducting meander to the device nominal area) up to 0.5. The patterned, 3.5-nm-thick nanostripes exhibited T_C's of above 10.7 K and J_C's on the order of $6–7 \times 10^6$ A/cm^2 at 4.2 K, essentially unsuppressed as compared to the plain film values. The above properties of the ultrathin NbN films, combined with the very high reproducibility of even $10 \times 10\ \mu m^2$ meanders, were the main advantage of using the RIE process rather than the earlier developed lift-off method. Figure 9.8 presents a completed SSPD structure at the end of a coplanar waveguide fabricated using the above procedure and a detailed scanning electron microscope (SEM) image of one of the meanders.

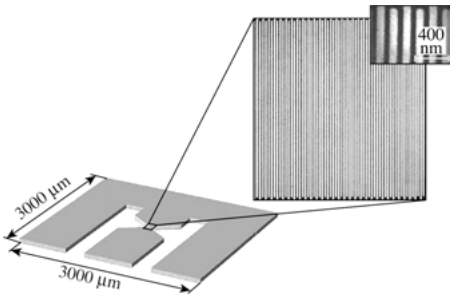

Fig. 9.8: Topology of SSPD contact pads forming a coplanar waveguide and an SEM image of the meander (NbN is black). The NbN nanostripe is ~70-nm wide (see inset in the SEM imagine), ~0.5-mm long, and covers a 10 μm × 10 μm area. [55]

9.3.2 Experimental characterization of SSPDs

A typical experimental setup for SSPD investigation and characterization is presented in Figure 9.9. There are several methods available for SSPD cooling, but the simplest one is to mount a device on a dipstick and immerse it directly in liquid helium in a standard storage Dewar. This method provides a very stable 4.2 K temperature and using, e.g., a 50-liter container, can assure at least one month of interrupted detector operation. For the most advanced applications, such as, e.g., virtually dark-count-free operation, an SSPD should be cooled to below 2 K (preferably to the 1.6–1.7 K range), which can be achieved by helium vapor evacuation in a dedicated optical cryostat, or one can use a specially designed cryoinsert for a standard storage container [9, 56]. Such an insert has a small capillary at its bottom that limits the rate of liquid helium intake into the sample chamber; in this way the helium pressure can be lowered only

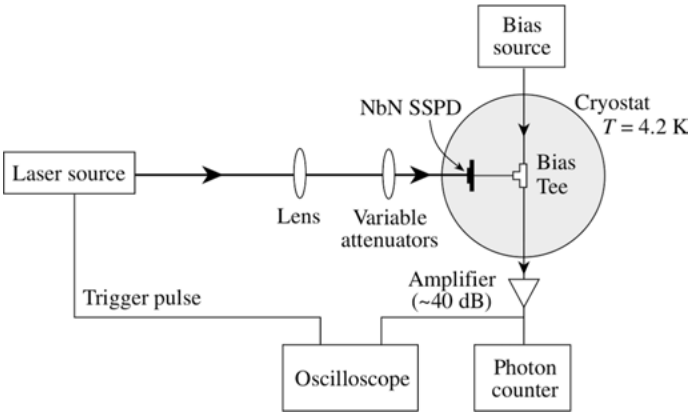

Fig. 9.9: Schematic setup of an SSPD experimental configuration.

inside the insert chamber, leading to a local temperature reduction. Another option, strongly favored in commercial applications and "turn-key" systems, is to implement a multistage cryorefrigerator with an optical access.

For photon-counting operation, an SSPD is typically DC-biased using a low-noise voltage source through a GHz-bandwidth bias-tee. The bias-tee allows for simultaneous DC biasing and a collection of ns-long voltage pulses generated as a result of photon absorption. The output pulses are next amplified and fed to read-out electronics. Typically, a room-temperature amplifier with a gain of 50 dB and bandwidth of 10 MHz to 2 GHz is enough to produce 100–500 mV pulses suitable for triggering most types of either photon counters or specialized, computer counting boards. In special applications, an SSPD is directly, in helium, connected to a cryogenic HEMT (High Electron Mobility Transistor) amplifier. In this configuration, the device is intended to operate as a photon-number-resolving sensor [58], or to study the origin of dark counts [59].

9.3.3 Demonstration of SSPD single-photon sensitivity and its detection efficiency

There are two basic approaches to demonstrate the single-photon response of a detector. The first is based on the splitting of the light emitted by a single-photon source into two beams and feeding them simultaneously to two identical SSPDs. Assuming that we have a pulsed source, obviously, in such an experiment only one detector can 'click' at a time, i.e., the rate of joint 'clicks' must be zero. This method unambiguously demonstrates that the detector is capable of registering single photons only when the source is truly a single-photon emitter. Otherwise there is some probability of two-, or even multiphoton events, resulting in coinciding clicks of the detectors, limiting applicability of the above approach. The second method which is based on an analysis of the statistics of the detector clicks is, actually, much more popular. In this case, we

need only one detector and can determine the minimal number of photons simultaneously incident on the detector that are required to trigger its positive response.

Classical light sources, such as lasers, light-emission diodes, etc., have a Poisson distribution of the number n of photons per pulse of the emitted radiation:

$$P(n) = m^n \exp(-m)/n! \tag{9.5}$$

where m is the mean number of photons per pulse. If $m \ll 1$, Equation (9.5) reduces to

$$P(n) = m^n/n! \tag{9.6}$$

Thus, under the ultraweak-incident-light illumination condition, if a single photon ($n = 1$) is sufficient to trigger a tested detector, its response, following Equation (9.6), is simply proportional to the mean number of photons per pulse ($P(1) = m$), or, in other words, to the mean power of the incoming light. Analogously, if the detector can be triggered only by pairs of photons ($n = 2$), its count rate will be proportional to the square of the mean incoming power ($P(2) = (m/2)^2$). For triple-photon events, the count rate is proportional to the cube of incoming power, etc. We see that based on the photon statistics of the source, by analyzing the slope (in the log-log scale) of the number of detector clicks versus the average light illumination power (in the ultraweak regime, where $m \ll 1$), we get direct information on the detector photon-counting capability, i.e., the actual number of photons required to trigger a detector response. This way one can prove that a given detector under test is a real single-photon counter. Figure 9.10 illustrates the above behavior for the very first published SSPD [1]. It plots the number of detector counts per second (left axis), or, equivalently, the probability (right axis) that the detector can produce an output voltage pulse, both as a function of the average number of photons per pulse, incident on the device area. We note that for the same detector, but biased at two different levels, for $I_B = 0.92 I_C$ and for very low photon fluxes, experimental data (open squares) show the linear decrease of the detection probability ($P = m$, as predicted by Equation (9.6)) for almost four orders of magnitude, clearly demonstrating the single-photon detection. At the same time, when this

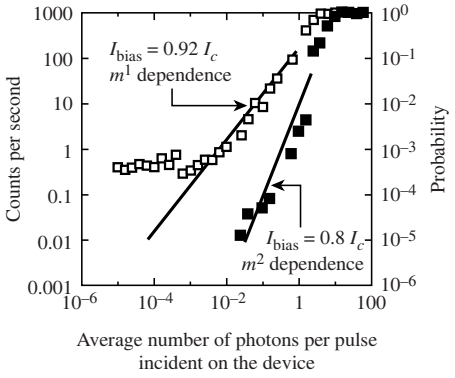

Fig. 9.10: Number of counts per second (left axis) recorded by the NbN SSPD and, equivalently, probability of the photon capture (right axis) versus the average number of photons per pulse incident upon the device, measured for two different bias current levels. The solid lines correspond to the theoretical prediction of Equation (9.6). The incident photon wavelength was 810 nm. [1]

device is operated under the same illumination conditions, but biased with $I_B = 0.8I_C$, experimental data points (closed squares) follow a quadratic dependence of detection probability, showing the two-photon detection. As expected, for two-photon events DE is significantly lower than for the single-photon detection. We also observe saturation of both dependences at high-incident photon fluxes, where probability is essentially one (all incident photons are recorded). Conversely, for ultrasmall fluxes, since the experiment was performed in an optically unshielded environment, single-photon-level dependence saturates at the level of $0.4\,s^{-1}$ counts, which can be regarded as the photon background of our laboratory. In the two-photon-level dependence, saturation is not observed, since the probability of two uncorrelated, stray photons hitting the device within its response duration is negligibly small.

In the above experiment, DE is defined as the ratio of photon counts N_{counts} of the detector to the number of incident photons $N_{photons}$ (see also a Footnote 2). N_{counts} can be directly measured by a frequency or pulse counter such as, e.g., Keysight 53131A, whereas the number of photons incident on the device is usually determined from power measurements. To achieve proper accuracy power measurements are performed at high photon fluxes (too high for single-photon counting) and then the beam is drastically attenuated by a bank of precisely calibrated optical attenuators and fed to the SSPD under test. In this case $N_{photons}$ is determined as follows:

$$N_{photons} = P/(\alpha\hbar\omega) \tag{9.7}$$

where P is measured power, α is attenuation, and $\hbar\omega$ is photon energy. More details on sources of errors in QE measurements can be found in [16].

As has been stressed in Section 9.2.1, the SSPD's ability to detect incident single photons depends very strongly on their energy, i.e., ability to form a large enough hot spot to trigger the detector's nanostripe, or, at least, its segment, into the transient resistive state. Thus, for a given detector, biased at a fixed I_B, we may or may not be able to observe a single-photon detection mechanism, depending on the energy of the incoming photons. The latter is very well illustrated in Figure 9.11 from [5] which shows that depending on the wavelength, i.e., energy, of the incident photons, the same detector, biased at a fixed I_B, can perform as either a single- or multiphoton detector. We can clearly see that, although, for a very low number of photons per pulse incident on the SSPD we observe in Figure 9.11 a single-photon detection regime ($n = 1$) for each studied wavelength, only for 405-nm radiation, the presence of at least one photon in the optical pulse is always sufficient to trigger the detector response. At the same time, near-infrared photons ($\lambda = 810$ nm and $\lambda = 1550$ nm), apparently, generate hot spots too small to ensure efficient single-photon SSPD operation, leading to enhanced probability of multiphoton detection with the increase of photon flux. Finally, for $\lambda = 1550$ nm radiation, SSPD multiphoton detection ($n \geq 2$) dominates.

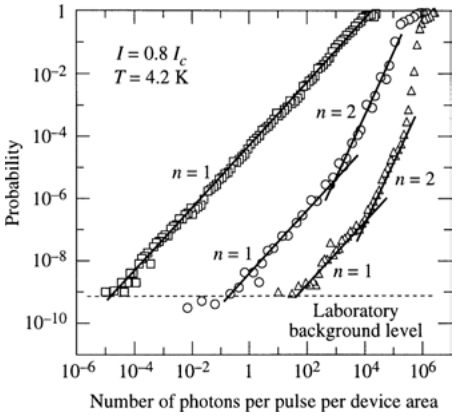

Fig. 9.11: Probability of photon counting versus the incident photon radiation flux for a $10 \times 10\ \mu m^2$, 10-nm-thick SSPD at 405-nm (squares), 810 nm (circles), and 1550-nm (triangles) wavelengths. The bias current was $I/I_C = 0.8$ and temperature was 4.2 K. The solid lines illustrate the slope exponents $n = 1$ and $n = 2$ [5].

9.3.4 Measurements of SSPD timing jitter

Timing jitter essentially defines the accuracy of photon arrival time resolution. For the jitter measurement one can use an experimental setup similar to the one shown in Figure 9.9 with a femtosecond, pulsed laser as a source with the oscilloscope being triggered using an electrical synchronization signal from the laser. The moment of time at which the SSPD photoresponse appears has some uncertainty since the photoresponse may sometimes appear earlier or later than the nominal arrival time of the femtosecond pulse. To characterize such an uncertainty quantitatively one may record the time distribution of the detection events. For this purpose, it is convenient to use the histogram-building feature of an oscilloscope to plot the time shift distribution of the rising edge of the response pulse as shown in Figure 9.12. The screenshot presented here was taken for a 1 μm-long nanostripe, characterized by a negligible L_k, and this is why the measured SSPD photoresponse signal has only 150-ps width at half-maximum. The corresponding width of the histogram of the rising edge arrival time (top part of the screen) represents timing jitter and is only 35 ps. In this case, the jitter measured by the oscilloscope is the whole system jitter τ_{total} comprised of the jitter of the electronics τ_{el} and the intrinsic jitter of the SSPD τ_{SSPD} and can be expressed as follows:

$$\tau_{total}^2 = \tau_{el}^2 + \tau_{SSPD}^2 \,. \tag{9.8}$$

Thus, the 35-ps value of the jitter presented in Figure 9.12 is the upper limit of our device.

Another method of jitter measurement is a traditional start-stop technique, often used in quantum optics experiments. In this case photoresponse pulses from either one or two identical SSPDs are fed to “start” and “stop” ports of a Time Correlated Single-Photon Counting (TCSPC) board. In the one-detector setup, an electrical trigger from a femtosecond laser is used as “start” and output from the SSPD is used as “stop”. When the two-detector setup is used, the optical beam of the laser is split into

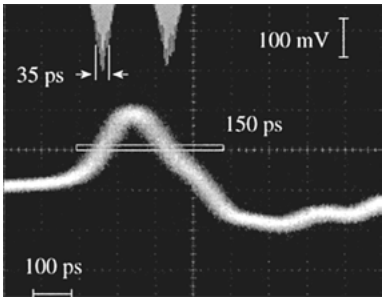

Fig. 9.12: Screenshot from a digital oscilloscope with a photoresponse pulse of a 1 μm-long SSPD with the histogram of the rising edge at the top of the screen. As a result of a very short length of the nanostripe, the L_k is negligible.

two parts and feeds two equal SSPDs. The photon-detection pulses from one SSPD are fed to the "start" channel of the TCSPC board and the output from a second SSPD is connected to the "stop" channel. The jitter measured this way is again the system jitter and is expressed, as before, by Equation (9.8). As before, measuring the SSPD jitter one should take into account the actual electrical noise of a given photon-counting system, e.g., amplifiers and the fact that reduction of I_B leads to an increase of the jitter due to limited amplifier gain [62].

It is worth noting that the physical nature of the timing jitter in SSPDs is not fully understood, although it must be related to the dynamics of the hot-spot formation and resulting occurrence of the resistive state, as indicated in [63]. Typically, in larger area, meander-type SSPDs, the reported values of the jitter are below 100 ps which is much better than in the case of any competing devices. Finally, it has been very recently reported [62] that proper optimization of the SSPD enables one to achieve a record-breaking 17.8 ps jitter, even in a commercial system.

9.3.5 Coupling of incoming light to SSPD as a method to increase system detection efficiency

To obtain the highest possible DE value, one needs, besides having an SSPD with a very high probability that the absorbed photon is counted, also to assure that all incident photons will be delivered to the nanostripe of the detector. This requirement is known as the problem of coupling SSPD to the incoming radiation. It is a nontrivial task and several approaches have been developed to reach coupling efficiency close to unity. The problem though is that electrodynamic parameters of the SSPD nanostripe that is responsible for light absorption are fixed by the requirement of maximum DE and turn out to be relatively far from optimal for good coupling. The width of the nanostripe is of order 100 nm or less, thus, it is much narrower than the incident light wavelength, leading to a creeping effect. The simplest approach and the one most often used is to flood the whole active area of the detector with light. In free-space systems, one needs to place the meander at the focal spot of the lens, while in the fiber-coupled configuration, the detector nanostripe has to be aligned against the fiber

core. Because the meander separation width is typically of order of the nanostripe itself (meander fill factor $f \approx 1/2$), for the incoming wave the detector is seen just as a continuous film with a total size much larger than the incident radiation wavelength. The absorption coefficient A of the superconducting film on a dielectric substrate is determined by its impedance Z at the optical frequency normalized to the impedance of free space $Z_0 = 377\,\Omega$ and the substrate index of refraction, and it is given by [1, Equation (1)]. Conversely, if our SSPD is fiber-coupled, we can consider that the refractive indexes of the media both in front of and behind the film are roughly the same and equal to n (good approximation for a detector coupled to a standard optical fiber and fabricated on Al_2O_3 or SiO_2 substrates), then the formula for A reads as

$$A = 4n\mathrm{Re}(Z_0/Z)/|2n + Z_0/Z|^2 \,. \tag{9.9}$$

An impedance of disordered metal films with a thickness of order several nm, as used for SSPD fabrication, is of order of 300–600 Ω, roughly corresponding to the surface resistance of a given film measured just above T_C (the order of magnitude is the same for a dc current as well as for frequencies corresponding to near IR). Actually, a patterned film can have substantially higher impedance for meanders with low f factors, and its impedance also depends on whether meander stripes have parallel or perpendicular orientation with respect to the polarization vector of the incoming wave [7]. For a typical case of an NbN meander fabricated on sapphire, with $f = 1/2$ and with 4-nm-thick strips perpendicularly oriented to the light polarization, Z can be assumed to be of the order of 500 Ω, leading to $A \approx 0.35$. The latter means that the resulting DE of this detector will not be greater than 35%, which is indeed the limitation for standard SSPDs. Simply, the rest of the incident photons are either transmitted or reflected by the metallic nanostripe.

Because the thickness of the superconducting nanostripe cannot be made greater (and hence Z cannot be made smaller) without a drastic decrease of IDE, the only way to overcome this limitation is to change the impedance of the space surrounding the stripe. Several approaches exist to accomplish this. The first is to incorporate an SSPD into a resonator-like structure by adding a quarter-wavelength layer and a mirror behind the meander. Such an approach has already been published in the literature and it results in an increase of the absorption coefficient up to 0.9 at the target wavelength [16]. Another approach is to fabricate periodic or aperiodic coupling structures with specially engineered refractive indices or impedances, in analogy to optical antennas.

Finally, one can replace the plane wave normally arriving at the strip with an evanescent mode of the wave that propagates in an optical waveguide (Figure 9.13). In this case, an optical waveguide is fabricated directly on top of the superconducting nanostripe, so the evanescent field outside the waveguide is absorbed by the stripe. If the interaction distance is long enough, the absorption will be close to unity. Actually, a waveguide-coupled SSPD has been demonstrated to have more than 0.99 absorption and the resulting SDE = 95% [64]. The main limitation of this approach is that the inci-

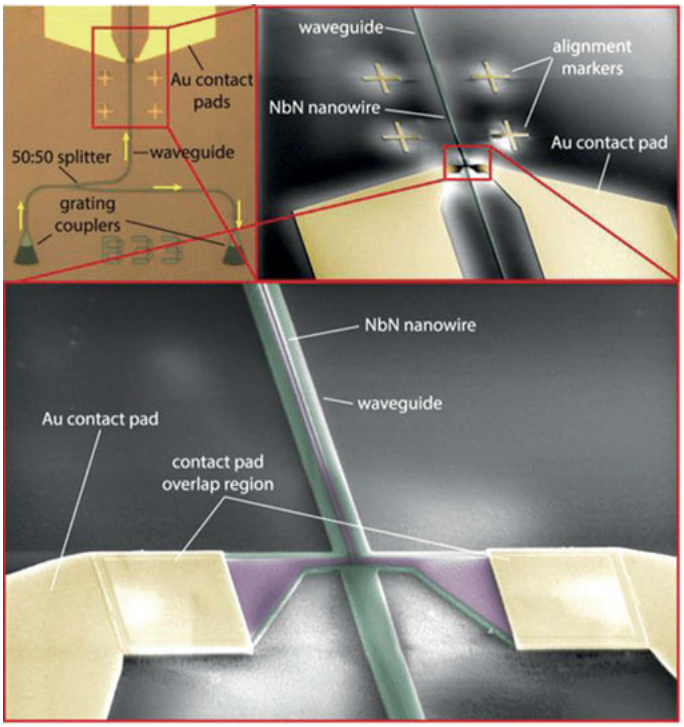

Fig. 9.13: Waveguide-integrated SSPD.

dent light either from free space or a fiber must be efficiently coupled to the waveguide. However, this would not be the case if a waveguide-coupled SSPD was part of an integrated photonic circuit, with the optical signal emitted directly into the waveguide. Hence, the waveguide-coupled SSPD is a very promising detector for integrated on-chip photonics devices – especially quantum computation hardware, which typically requires near-unity detection efficiency.

9.4 Conclusion and future research directions

This chapter focused on fundamental properties of practical SSPDs and presented the basic physical models of their operation. Since its discovery in 2001 [1], very extensive research has been published, covering both the theoretical and experimental aspects of SSPD operation, and, as we have demonstrated here, there is a quite good understanding of the physical mechanisms behind SSPD photoresponse dynamics, as well as of the origin of dark counts. However, future studies of detector operation are still needed to gain deeper understanding. The most demanding problem is the development of a complete, quantitative theory that could use material parameters such as

mean path length, T_c, Ω_D, E_F, Δ, $N(0)$ and, subsequently, be able to predict whether a superconducting stripe with given dimensions (thickness and width) and geometry (e.g., single stripe or meander structure) is capable of detecting a single photon and if yes, in what spectral range of the incident radiation for the maximized current bias. This theory should include both e–e and e–ph interactions, diffusion of quasiparticles, and the equation for Δ.

From the experimental point of view, it would be interesting to know in detail the dependence of IDE on I_B in weak magnetic fields and how it changes for detectors made from different superconductors, including ferromagnet-superconductor nanobilayers [65, 66]. Existing results [36, 39] for NbN and MoSi detectors show that the hot spot in practical devices always has a size that is significantly smaller than the nominal width of the stripe. It would be interesting to perform similar experiments with WSi-, NbC-, NbTiN- or TaN-based SSPDs and, hopefully, clarify the question about the actual size of the hot spot in nanostripes fabricated from these materials and how it relates to the stripe width.

Extension of the SSPD single-photon operation to mid- or even far-infrared radiation is another great challenge. This requires, on the one hand, the above-mentioned input from theory to choose an appropriate material, and, on the other hand, significantly improved fabrication technology, resulting in very highly uniform nanostripes with a width that is as narrow as possible.

In this chapter we do not discuss any specific SSPD applications, however, SSPDs are currently the device-of-choice for most advanced, high-performance applications, and have demonstrated excellent properties in many areas in both classical and quantum optics. The most advanced implementations are in optical time-domain reflectometry [67], laser ranging (LiDAR) [68], space-to-ground quantum communications [69, 70], quantum dot photonics [71, 72], quantum key distribution [73], as well as in experiments with indistinguishable and entangled photon pairs [74, 75], and, finally, there is rapidly growing interest for using SSPDs in life sciences [76].

One of the most urgent problems in all the above-mentioned fields is the development of highly efficient couplers for light feed from optical sources and/or fibers into the SSPD, as well as an SSPD array design for imaging systems. In many imaging spectroscopy applications, using single-photon detector arrays, would drastically improve system performance, by providing unique, detailed information on very weak photon sources. For current SSPD array systems, the main problem is, unfortunately, a relatively low yield of good devices that significantly limits the number of active array elements, as well as the lack of fast read-out of any given array pixel, especially for large arrays. One of the most promising solutions here could be the direct integration (in a cryogenic environment) of the SSPD array with a superconducting read-out processing circuit. A good example is the recent demonstration of successful SSPD integration with the Josephson-junction-based, rapid single flux quantum (RSFQ) logic [77].

Acknowledgment: Research in Rochester has been supported in part by the grant from HYPRES Co., and by the New York State Advanced Technology Centers for Innovative and Enabling Technologies (University of Rochester) and Advanced Sensor Technologies (Stony Brook University). R.S. also acknowledges the European Union COST Action MP1201. Research in Moscow was supported by the grant (State Contract) 14.B25.31.0007 from the Russian Ministry of Education and Science. D.V. acknowledges support from the Russian Foundation for Basic Research, project 15-42-02365.

Bibliography

[1] Gol'tsman G, Okunev O, Chulkova G, Lipatov A, Semenov A, Smirnov K, Voronov B, Dzardanov A, Williams C, Sobolewski R. "Picosecond superconducting single-photon optical detector", Appl. Phys. Lett. 79:705–707, 2001.

[2] Semenov AD, Gol'tsman GN, Korneev AA. Quantum detection by current carrying superconducting film, Physica C (Amsterdam) 351:349, 2001.

[3] Gol'tsman GN, Okunev O, Chulkova G, Lipatov A, Semenov A, Smirnov K, Voronov B, Dzardanov A, Williams C, Sobolewski R. "Fabrication and Properties of an Ultrafast NbN Hot-Electron Single Photon Detector," IEEE Trans. Appl. Supercon. 11:574–577, 2001.

[4] Gol'tsman GN, Smirnov K, Kouminov P, Voronov B, Kaurova N, Drakinsky V, Zhang J, Verevkin A, and Roman Sobolewski «Fabrication of Nanostructured Superconducting Single-Photon Detectors» Trans IEEE. Appl. Supercon. 13:192–195, 2003.

[5] Sobolewski R, Verevkin A, Gol'tsman GN, Lipatov A, Wilsher K. "Ultrafast Superconducting Single-Photon Optical Detectors and Their Applications," IEEE Trans. Appl. Supercon. 13:1151–1157, 2003.

[6] Hu X, Zhong T, White JE, Dauler EA, Najafi F, Herder CH, Wong FNC, Berggren KK. «Fiber-coupled nanowire photon counter at 1550 nm with 24% system detection efficiency», Optics Letters 34(23):3607, 2009.

[7] Dorenbos SN, Reiger EM, Akopian N, Perinetti U, Zwiller V, Zijlstra T, Klapwijk TM. "Superconducting single photon detectors with minimized polarization dependence" Appl. Phys. Lett. 93:161102, 2008.

[8] Ejrnaes M, Cristiano R, Gaggero A, Mattioli F, Leoni R, Voronov B, Gol'tsman G. «A cascade switching superconducting single photon detector» Appl. Phys. Lett. 91:262509, 2007.

[9] www.scontel.ru.

[10] Semenov A, Engel A, Il'in K, Gol'tsman G, Siegel M, Hübers H-W. "Ultimate performance of a superconducting quantum detector", Eur. Phys. J. AP 21:171–178, 2003.

[11] Dorenbos SN, Reiger EM, Perinetti U, Zwiller V, Zijlstra T, Klapwijk TM. Low noise superconducting single photon detectors on silicon Appl. Phys. Lett. 93:131101, 2008.

[12] Miki S, Takeda M, Fujiwara M, Sasaki M, Otomo A, Wang Z. Superconducting NbTiN nanowire single photon detectors with low kinetic inductance Appl. Phys. Express 2:075002, 2009.

[13] Seleznev VA, Tarkhov MA, Voronov BM, Milostnaya II, Lyakhno VYu, Garbuz AS, Mikhailov MYu, Zhigalina OM, Gol'tsman GN. "Deposition and characterization of few-nanometers-thick superconducting Mo–Re films" Supercond. Sci. Technol. 21:115006, 2008.

[14] Engel A, Aeschbacher A, Inderbitzin K, Schilling A, Il'in K. Tantalum nitride superconducting single-photon detectors with low cut-off energy. Appl. Phys. Lett 100:062601, 2012.

[15] Shibata H, Asahi M, Maruyama T, Akazaki T, Takesue H, Honjo T, Tokura Y. Optical response and fabrication of MgB_2 nanowire detectors IEEE Trans. Appl. Supercond. 19:358–360, 2009.

[16] Marsili F, Verma VB, Stern JA, Harrington S, Lita AE, Gerrits T, Vayshenker I, Baek B, Shaw MD, Mirin RP, Nam SW. "Detecting single infrared photons with 93% system efficiency", Nature Photonics. vol 7 210–214 (2013).
[17] Korneeva YuP, Mikhailov MYu, Pershin YuP, Manova NN, Divochiy AV, Vakhtomin YuB, Korneev AA, Smirnov KV, Sivakov AG, Devizenko AYu, Goltsman GN. "Superconducting single-photon detector made of MoSi film" Supercond. Sci. Technol. 27:095012, 2014.
[18] Langer JS, Ambegaokar V. "Intrinsic resistive transition in narrow superconducting channels," Phys. Rev., vol. 164, pp. 498–510, 1967.
[19] McCumber DE, Halperin BI. "Time scale of intrinsic resistive fluctuations in thin superconducting wires," Phys. Rev. B 1:1054–1070, 1970.
[20] Engel A, Semenov A, Heubers H-W, Il'in K, Siegel M. "Fluctuation effects in superconducting nanostrips," Physica C: Superconductivity and its Applications, vol. 444, pp. 12–18, Sep 2006.
[21] Nasti U, Parlato L, Ejrnaes M, Cristiano R, Taino T, Myoren H, Roman Sobolewski, Pepe G. "Thermal fluctuations in superconductor/ferromagnet nanostripes," Phys. RevB 92:014501, 2015.
[22] Somani S, Kasapi S, Wilsher K, Lo W, Sobolewski R, Gol'tsman GN. "New photon detector for device analysis: Superconducting single-photon detector based on a hot electron effect", J. Vac. Sci. Technol. B 19, No. 6:2766–2769, 2001.
[23] Natarajan C, Tanner MG, Hadfield RH. "Superconducting nanowire single-photon detectors: physics and applications" Supercond. Sci. Technol. 25:063001, 2012.
[24] Ovchinnikov YuN, Kresin VZ. Nonstationary state of superconductors: Application to nonequilibrium tunneling detectors Phys. Rev. B 58(12):416, 1998.
[25] Kozorezov AG, Volkov AF, Wigmore JK, Peacock A, Poelaert A. and R. den Hartog, Quasiparticle-phonon downconversion in nonequilibrium superconductors, Phys. Rev. B 61(11):807, 2000.
[26] Van Vechten D, Wood K. Probability of quasiparticle self-trapping due to localized energy deposition in nonequilbrium tunnel-junction detectors, Phys. Rev. B 43(12):852, 1991.
[27] Clem JR, Berggren KK. Geometry-dependent critical currents in superconducting nanocircuits, Phys. Rev. B 84:174510, 2011.
[28] Zotova AN, Vodolazov DY. Photon detection by current-carrying superconducting film: A time-dependent Ginzburg–Landau approach, Phys. Rev. B 85:024509, 2012.
[29] Zotova AN, Vodolazov DY. Intrinsic detection efficiency of superconducting nanowire single photon detector in the modified hot spot model, Supercond. Sci. Technol. 27:125001, 2014.
[30] Vodolazov DYu. Current dependence of the red boundary of superconducting single-photon detectors in the modified hot-spot model, Phys. Rev. B 90:054515, 2014.
[31] Semenov A, Engel A, Hubers H-W, Il'in K, Siegel M. Spectral cut-off in the efficiency of the resistive state formation caused by absorption of a single-photon in current-carrying superconducting nano-strips, Eur. Phys. J. B 47:495, 2005.
[32] Eftekharian A, Atikian H, Majedi AH. Plasmonic superconducting nanowire single photon detector Opt. Express 21:3043, 2013.
[33] Engel A, Schilling A. Numerical analysis of detection-mechanism models of superconducting nanowire single-photon detector, J. Appl. Phys. 114:214501, 2013.
[34] Engel A, Lonsky J, Zhang X, Schilling A. Detection Mechanism in SNSPD: Numerical Results of a Conceptually Simple, Yet Powerful Detection Model, IEEE Trans. Appl. Supercon. 25:2200407, 2015.
[35] Rothwarf A, Taylor BN. Measurement of Recombination Lifetimes in Superconductors, Phys. Rev. Lett. 19:27, 1967.
[36] Bulaevskii LN, Graf MJ, Kogan VG. Vortex-assisted photon counts and their magnetic field dependence in single-photon superconducting detectors, Phys. Rev. B 85:014505, 2012.

[37] Vodolazov DYu, Korneeva YuP, Semenov AV, Korneev AA, Goltsman GN. Vortex-assisted mechanism of photon counting in superconducting nanowire single photon detector revealed by external magnetic field, Phys. Rev. B 92:104503, 2015.
[38] Renema JJ, Wang Q, Gaudio R, Komen I, op't Hoog K, Sahin D, Schilling A, van Exter MP, Fiore A, Engel A, de Dood MJA. Position-Dependent Local Detection Efficiency in a Nanowire Superconducting Single-Photon Detector, Nano Lett. 15:4541, 2015.
[39] Korneev AA, Korneeva YP, Mikhailov MY, Pershin YP, Semenov AV, Vodolazov DY, Divochiy AV, Vakhtomin YB, Smirnov KV, Sivakov AG, Devizenko AY, Goltsman GN. Characterization of MoSi superconducting single-photon detectors in the magnetic field, IEEE Trans. Appl. Supercon. 25:2200504, 2015.
[40] Lusche R, Semenov A, Korneeva Y, Trifonov A, Korneev A, Gol'tsman G. and H.-W. Hübers, Effect of magnetic field on the photon detection in thin superconducting meander structures, Phys. Rev. B 89:104513, 2014.
[41] Semenov A, Charaev I, Lusche R, Ilin K, Siegel M, Hübers H-W, Bralović N, Dopf K, Vodolazov DYu. Asymmetry in the effect of magnetic field on photon detection and dark counts in bended nanostripes, Phys. Rev. B 92:174518, 2015.
[42] Kitaygorsky J, Komissarov I, Jukna A, Minaeva O, Kaurova N, Korneev A, Voronov B, Milostnaya I, Gol'tsman G, Sobolewski R. "Dark Counts in Nanostructured NbN Superconducting Single-Photon Detectors and Bridges,", IEEE Trans. Appl. Supercon. 17, No. 2:275–278, 2007.
[43] Yamashita T, Miki S, Qiu W, Fujiwara M, Sasaki M, Wang Z. "Temperature Dependent Performances of Superconducting Nanowire Single-Photon Detectors in an Ultralow-Temperature Region" Appl. Phys. Express 3:102502, 2010.
[44] Bartolf H, Engel A, Schilling A, Ilin K, Siegel M, Hübers HW, Semenov A. "Current-assisted thermally activated flux liberation in ultrathin nanopatterned NbN superconducting meander structures", Phys. Rev. B 81:024502, 2010.
[45] Bulaevskii LN, Graf MJ, Batista CD, Kogan VG. "Vortex-induced dissipation in narrow current-biased thin-film superconducting strips" Physical Review B 83:144526, 2011.
[46] Vodolazov DY. "Saddle point states in two-dimensional superconducting films biased near the depairing current", Phys. Rev. B 85:174507, 2012.
[47] Korneev A, Matvienko V, Minaeva O, Milostnaya I, Rubtsova I, Chulkova G, Smirnov K, Voronov B, Golt'sman G, Slysz W, Pearlman A, Verevkin A, Sobolewski R. "Quantum efficiency and noise equivalent power of nanostructured, NbN, single-photon detectors in the wavelength range from visible to infrared", IEEE Trans. on Appl. Supercond. 15(2):571–574, 2005.
[48] Murphy A, Semenov A, Korneev A, Korneeva Yu, Gol'tsman G, Bezryadin A. "Three Temperature Regimes in Superconducting Photon Detectors: Quantum, Thermal and Multiple Phase-Slips as Generators of Dark Counts" Scientific Reports 5:10174, 2015.
[49] Kurkijärvi J. Intrinsic Fluctuations in a Superconducting Ring Closed with a Josephson Junction. Phys. Rev. B. 6:832, 1972.
[50] Slysz W, Wegrzecki M, Bar J, Gorska M, Zwiller V, Latta C, Bohi P, Milostnaya I, Minaeva O, Antipov A, Okunev O, Korneev A, Smirnov K, Voronov B, Kaurova N, Gol'tsman G, Pearlman A, Cross A, Komissarov I, Verevkin A, Sobolewski R. "Fiber-coupled single-photon detectors based on NbN superconducting nanostructures for practical quantum cryptography and photon-correlation studies", Appl. Phys. Lett. 88:261113, 2006.
[51] Smirnov KV, Divochiy AV, Vakhtomin YuB, Sidorova MV, Karpova UV, Morozov PV, Seleznev VA, Zotova AN, Vodolazov DYu. Rise time of voltage pulses in NbN superconducting single photon detectors, Appl. Phys. Lett. 109:052601, 2016.
[52] Tarkhov M, Claudon J, Poizat JPh, Korneev A, Divochiy A, Minaeva O, Seleznev V, Kaurova N, Voronov B, Semenov AV, Gol'tsman G. "Ultrafast reset time of Superconducting Single Photon Detectors" Appl. Phys. Lett., Vol.92, Issue 24, 2008.

[53] Baek B, Lita AE, Verma V, Nam SW. "Superconducting a-W_xSi_{1-x}a-W_xSi_{1-x} nanowire single-photon detector with saturated internal quantum efficiency from visible to 1850 nm" Appl. Phys. Lett. 98:251105–251103, 2011.
[54] Gol'tsman GN, Smirnov K, Kouminov P, Voronov B, Kaurova N, Drakinsky V, Zhang J, Verevkin A, Sobolewski R. "Fabrication of Nanostructured Superconducting Single-Photon Detectors", IEEE Transactions On Applied Superconductivity 13(2):192–195, 2003.
[55] Gol'tsman G, Minaeva O, Korneev A, Tarkhov M, Rubtsova I, Divochiy A, Milostnaya I, Chulkova G, Kaurova N, Voronov B, Pan D, Kitaygorsky J, Cross A, Pearlman A, Komissarov I, Slysz W, Wegrzecki M, Grabiec P, Sobolewski R. Middle-Infrared to Visible-Light Ultrafast Superconducting Single-Photon Detectors, IEEE Trans on Appl Supercond 17:246, 2007.
[56] Korneev A, Vachtomin Y, Minaeva O, Divochiy A, Smirnov K, Okunev O, Gol'tsman G, Zinoni C, Chauvin N, Balet L, Marsili F, Bitauld D, Alloing B, Lianhe Li; Fiore A, Lunghi L, Gerardino A, Halder M, Jorel C, Zbinden H. "Single-Photon Detection System for Quantum Optics Applications". IEEE Journal ofSelected Topics in Quantum Electronics 13(4):944–995, 2007.
[57] Verevkin A, Pearlman A, Slysz W, Zhang J, Currie M, Korneev A, Chulkova G, Okunev O, Kouminov P, Smirnov K, Voronov B, Gol'tsman G, Sobolewski R. "Ultrafast superconducting single-photon detectors for near-infrared wavelength quantum communications", Journal of Modern Optics 51(9–10):1447–1458, 2004.
[58] Bell MG, Antipov A, Karasik B, Sergeev A, Mitin V, Verevkin A. "Photon number-resolved detection with sequentially connected nanowires", IEEE Trans. Appl. Supercond. 17:289–292, 2007.
[59] Kitaygorsky J, Dorenbos S, Reiger E, Schouten R, Zwiller V, Sobolewski R. "HEMT-based Read-Out Technique for Dark and Photon Count Studies in NbN Superconducting Single-Photon Detectors," IEEE Trans. Appl. Supercon. 19:346–349, 2009.
[60] Kitaygorsky J, Słysz W, Shouten R, Dorenbos S, Reiger E, Zwiller V, Sobolewski R. "Amplitude distributions of dark counts and photon counts in NbN superconducting single-photon detectors integrated with the HEMT readout," Physica C 532:33–39, 2017.
[61] Sobolewski R, Zhang J, Slysz W, Pearlman A, Verevkin A, Lipatov A, Okunev O, Chulkova G, Korneev A, Smirnov K, Kouminov P, Voronov B, Kaurova N, Drakinsky V, Gol'tsman GN. "Ultrafast Superconducting Single-Photon Optical Detectors." In: Spigulis J, Teteris J, Ozolinsh M, Lusis A (eds). Advanced Optical Devices, Technologies, and Medical Applications. Proc. of SPIE Vol. 5123, 1–11, 2003.
[62] You L, Yang X, He Y, Zhang W, Liu D, Zhang W, Zhang L, Zhang L, Liu X, Chen S, Wang Z, Xie X. "Jitter analysis of a superconducting nanowire single photon detector" AIP Advances 3:072135, 2013.
[63] Zhang J, Slysz W, Verevkin A, Sobolewski R, Okunev O, Gol'tsman GN. "Time Delay of the Resistive State Formation in Superconducting NbN Stripes Illuminated by Single Optical Photons," Phys. Rev. B 67(13):132508-1–132508-4, 2003.
[64] Kahl O, Ferrari S, Kovalyuk V, Goltsman GN, Korneev A, Pernice WHP. "Waveguide integrated superconducting single-photon detectors with high internal quantum efficiency at telecom wavelengths" Scientific Reports 5:10941, 2015.
[65] Marrocco N, Pepe GP, Capretti A, Parlato L, Pagliarulo V, Peluso G, Barone A, Cristiano R, Ejrnaes M, Casaburi A, Kashiwazaki N, Taino T, Myoren H, Sobolewski R. "Strong critical current density enhancement in NiCu/NbN superconducting nanostripes for optical detection," Appl. Phys. Lett. 97:092504, 2010.
[66] Nasti U, Parlato L, Ejrnaes M, Cristiano R, Taino T, Myoren H, Sobolewski R, Pepe G. "Thermal Fluctuations in superconductor/ferromagnet nanostripes," Phys. Rev. B 92:014501, 2015.

[67] Zhao Q, Xia L, Wan C, Hu J, Jia T, Gu M et al. "Long-haul and high-resolution optical time domain reflectometry using superconducting nanowire single-photon detectors" Sci Rep 5:10441, 2015.
[68] McCarthy A, Krichel N, Gemmell N. "Kilometer-range, high resolution depth imaging via 1560 nm wavelength single-photon detection" Opt Express 21:8904–8915, 2013.
[69] Boroson DM. "Overview of the Lunar Laser Communication Demonstration" Icsos 9:7, 2014.
[70] Wilson KE, Antsos D, Roberts LC Jr, Piazzolla S, Clare LP. Croon "Development of the Optical Communications Telescope Laboratory: A Laser Communications Relay Demonstration Ground Station" Proc. International Conference on Space Optical Systems and Applications (ICSOS), 2012, http://icsos2012.nict.go.jp/pdf/1569604591.pdf.
[71] Correa RE, Dauler EA, Nair G, Pan SH, Rosenberg D, Kerman AJ et al. "Single photon counting from individual nanocrystals in the infrared" Nano Lett 12:2953–2958, 2012.
[72] Bose R, Sridharan D, Kim H, Solomon GS, Waks E. "Low-photon-number optical switching with a single quantum dot coupled to a photonic crystal cavity" Phys Rev Lett 108:1–5, 2012.
[73] Takesue H, Nam SW, Zhang Q, Hadfield R, Honjo T, Tamaki K, Yamamoto Y. "Quantum key distribution over a 40-dB channel loss using superconducting single-photon detectors" Nat. Photonics 1:343–348, 2007.
[74] Shalm LK, Meyer-Scott E, Christensen BG, Bierhorst P, Wayne MA, Stevens MJ et al. "Strong Loophole-Free Test of Local Realism" Phys Rev Lett 115:1–10, 2015.
[75] Hamel DR, Shalm LK, Hübel H, Miller AJ, Marsili F, Verma VB et al. "Direct generation of three-photon polarization entanglement", Nat Photonics 8:801–807, 2014.
[76] Yamashita T, Liu D, Miki S, Yamamoto J, Haraguchi T, Kinjo M et al. "Fluorescence correlation spectroscopy with visible-wavelength superconducting nanowire single-photon detector" Opt Express 22:28783–28789, 2014.
[77] Hofherr M, Wetzstein O, Engert S, Ortlepp T, Berg B, Ilin K, Henrich D, Stolz R, Toepfer H, Meyer H-G, Siegel M. "Orthogonal sequencing multiplexer for superconducting nanowire single-photon detectors with RSFQ electronics readout circuit" Opt Express 27:28683, 2012.